$MgNb_2O_6$ Modified $K_{0.5}Na_{0.5}NbO_3$ Eco-Piezoceramics: Scalable Processing, Structural Distortion and Complex Impedance at Resonance

Antonio Iacomini,*[a] Sebastiano Garroni,[a] Nina Senes,[a] Gabriele Mulas,[a] Stefano Enzo,[a] Matteo Poddighe,[a] Álvaro García,[b] José F. Bartolomé,[b] and Lorena Pardo[b]

In this work, piezoceramics of the lead-free composition $K_{0.5}Na_{0.5}NbO_3$ with an increasing amount of $MgNb_2O_6$ (0, 0.5, 1, 2 wt.%) were prepared through conventional solid-state synthesis and sintered in air atmosphere at 1100 °C. The effect of magnesium niobate addition on structure, microstructure and piezoelectric properties was evaluated. The ceramics maintain the orthorhombic Amm2 phase for all compositions, while an orthorhombic Pbcm secondary phase was found for increasing the concentration of $MgNb_2O_6$. Our results show that densification of these ceramics can be significantly improved up to 94.9% of theoretical density by adding a small amount of magnesium-based oxide (1 wt.%). Scanning electron microscopy morphology of the 1 wt.% system reveals a well-packed structure with homogeneous grain size of ~2.72 μm. Dielectric and piezoelectric properties become optimal for 0.5–1.0 wt.% of $MgNb_2O_6$ that shows, with respect to the unmodified composition, either higher piezoelectric coefficients, lower anisotropy and relatively low piezoelectric losses ($d_{33} = 97$ pC N^{-1}; $d_{31} = -36.99$ pC N^{-1} and $g_{31} = -14.04 \times 10^{-3}$ mV N^{-1}; $Q_p(d_{31}) = 76$ and $Q_p(g_{31}) = 69$) or enhanced electromechanical coupling factors ($k_p = 29.06$% and $k_{31} = 17.25$%).

1. Introduction

$Pb(Zr_{1-x}Tix)O_3$ (PZT) and PZT-based ferro-piezoelectric ceramics are, today, the most commercially exploited systems due to their dielectric, piezoelectric and electromechanical coupling coefficients suitable for a wide number of classical technological applications such as buzzers, gas ignitors, sensors, ultrasonic motors and so on.[1] However, the high toxicity of lead oxide, commonly used as reagent in PZT preparation (up to 60 wt.%), has moved the attention for alternative systems which could replace lead-based materials while miming their performance in emerging applications.[2–5] Among them, sodium potassium niobate, $K_{1-x}Na_xNbO_3$ (KNN) is one of the most promising and widely studied lead-free system with high Curie Temperature (420 °C), good ferroelectric properties ($Pr = 33\ \mu C\,cm^{-2}$) and appealing electromechanical planar coupling factor for $x = 0.5$.[6]

[a] A. Iacomini, Prof. S. Garroni, Dr. N. Senes, Prof. G. Mulas, Prof. S. Enzo, M. Poddighe
Department of Chemistry and Pharmacy
University of Sassari
Via Vienna 2
07100 Sassari (Italy)
E-mail: aiacomini@uniss.it
[b] Á. García, Dr. J. F. Bartolomé, Prof. L. Pardo
Instituto de Ciencia de Materiales de Madrid (ICMM)
Consejo Superior de Investigaciones Científicas (CSIC)
c/ Sor Juana Ines de la Cruz
Cantoblanco, 28049 Madrid (Spain)

Supporting information for this article is available on the WWW under https://doi.org/10.1002/open.202100089

On the other hand, KNN still present some disadvantages related with their preparation and, in particular, with the extremely narrow interval of temperatures for sintering, high volatility of light elements, and poor densification which affect the piezo properties.[7] To overcome these drawbacks, soft chemical routes, like hydrothermal, microwave assisted and sol-gel methods, have been explored during the last years. On the other hand, solid-state reaction route followed by air sintering still remains the most common, easiest and cheapest method.[8,9] Recently, some efforts have been made to improve the scalability of the manufacturing process, which is still an open issue for KNN ceramics. In this context, the mechano-chemical activation has aroused particular interest due to its many benefits including shorter synthesis time, enhanced chemical homogeneity and density of sintered pellets.[10] In addition, over the years, various "additives" have been suggested to increase the densification and lower the sintering temperature of KNN-based ceramics. In particular, Cu^{2+} and Zn^{2+} based oxides such as CuO, $K_4CuNb_8O_{23}$, $CuNb_2O_6$, $K_{5.4}Cu_{1.3}Ta_{10}O_{29}$, ZnO and $K_{1.94}Zn_{1.05}Ta_{5.19}O_{15}$, have proved to effectively promote densification through the formation of a secondary phase during sintering.[11–16] Furthermore, it is frequently reported that these modifying agents, in particular Cu-based compounds, act as acceptors dopants that create anion (oxygen) vacancies and associated defect dipoles. Due to the high mobility of the oxygen vacancies, the defect dipoles are easily oriented by the external field and make difficult the overall switching of the polarization. This domain wall pinning effect is responsible to the increase of the "hard" behavior of the ceramics.[17–19]

Likewise, Mg-based compounds have shown beneficial effects on the sintering performance of KNN through the

formation of a liquid phase, which favor the mass transportation then promoting the densification process. Furthermore, the addition of MgO seems to enhance the electrical properties of the KNN-modified ceramics ($d_{33} > 100$ pC N^{-1}; $k_p > 30\%$; $\varepsilon^T_{33} > 600$).[20] Nevertheless, unlike to the Cu/Zn-based additives, Mg-based systems have been poorly explored, up to know, on KNN ceramics.

In this work, $MgNb_2O_6$ (hereinafter abbreviated as MN) was tested on KNN ceramics, for the first time by our knowledge. The synthesis was conducted with the mechanochemical-assisted activation method, which is an easy and scalable process. The effect of MN on sintering behavior, structure, microstructure, and piezoelectric, elastic and dielectric properties at resonance have been evaluated.

2. Results and Discussion

In this study, the composition $K_{0.5}Na_{0.5}NbO_3$ was selected due its highest piezoelectric properties. The density of the as-prepared KNN ceramics, sintered at 1100 °C, as a function of MN concentration (wt.%) is summarized in Figure 1. With the increasing of MN content, the density firstly increased from 4.02 g cm^{-3} (pure KNN) to 4.10 g cm^{-3} (MN 0.5 wt.%), until reaching an optimal value of 4.28 g cm^{-3} for the sample modified with 1 wt.%, corresponding to 94.9% of the theoretical density (TD) of pure KNN (4.51 g cm^{-3}).[21]

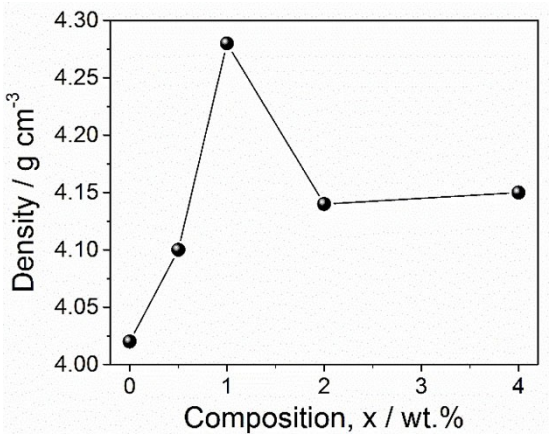

Figure 1. Density Vs composition of KNN-xMN series.

For higher amount of MN (2 wt.%), the density decreased to 4.14 g cm^{-3}, in accordance with trends reported in the current literature for other KNN-modified systems.[22,23] The system with 4 wt.% of MN, exhibits a similar density with respect to 2 wt.%, but it resulted too conductive for determining its electromechanical properties, most probably due to the presence of secondary phases segregated at the grain boundaries.[24] For this reason, the structural and microstructural characterization has been carried out only for the 0.5, 1 and 2 wt.% modified systems, together with the pure KNN for comparison purposes. Starting from the crucial point that the structures of piezoceramics significantly influence their properties, the XRD patterns of calcined KNN and sintered KNN-xMN (x = 0, 0.5, 1, 2 wt.%), at room temperature, were recorded to get light on their structure. The as-calcined pure KNN pattern appears as a complex multiphase mixture (Figure 2).

The Rietveld refinement were performed using the orthorhombic Amm2 $KNbO_3$, the tetragonal P4mm $K_{0.3}Na_{0.7}NbO_3$ and the orthorhombic Pbcm $NaNbO_3$ as a starting model, according to what reported by other authors (Figure 2a).[10,25] The good agreement between the model and the experimental data was established by the low R-factor (Rwp = 6.91%) achieved by this analysis. Shoulders on the right side of the peaks are attributable to the orthorhombic Pbcm phase of the $NaNbO_3$ (Figure 2b). The presence of mixed phases was due to the monoclinic polymorph of Nb_2O_5 used as starting reagent (Figure S1 in the Supporting Information) in the solid-state reaction, in agreement with what was observed by Hreŝĉak et al.[26] The milled monoclinic Nb_2O_5 formed an inhomogeneous mixture of solid solutions with various Na:K ratios.

The estimated cell volumes here evaluated for the orthorhombic Amm2, the tetragonal P4mm and the orthorhombic Pbcm phases (Table S1 in the Supporting Information) are slightly different compared to the corresponding values reported in the literature for purely stoichiometric compounds. In particular, we observed a shrinkage of $KNbO_3$ and an expansion of $NaNbO_3$ and $K_{0.3}Na_{0.7}NbO_3$ unit cell volumes. This evidence suggests that a partial diffusion of Na^+ and K^+ into $KNbO_3$ and $NaNbO_3$ respectively take place during calcination. This may be justified by the smaller Na^+ radius (rNa = 1.02 Å) compared to K^+ (rK = 1.38 Å). Since the reaction rate of Na_2CO_3/

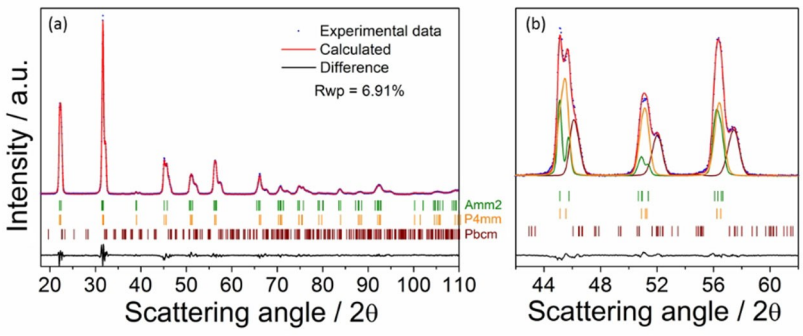

Figure 2. (a) XRD pattern and Rietveld refinement of calcined KNN powders. (b) Magnification of the diffraction peaks between 42 and 62°.

Nb_2O_5 is one order of magnitude higher than K_2CO_3/Nb_2O_5, it is reasonable to expect that the average crystallite size dimensions will be larger for $NaNbO_3$ (2000 Å vs 1115 Å). At the same time, the micro-strain generated by the presence of K^+ in the $NaNbO_3$ unit cell is about twice compared to $KNbO_3$ (Table S1 in the Supporting Information). The tetragonal P4mm, which is the majority phase in the powder mixture, shows a slightly larger cell volume (63.773 $Å^3$) compared to the stoichiometry composition (62.572 $Å^3$), suggesting that this phase probably contain a larger amount of potassium than the nominal composition.

The XRD analyses of sintered pellets are reported in Figure 3. All ceramics possessed the typical perovskite-type structure. For $x<1$ a tetragonal tungsten-bronze type phase has been detected in trace (see details of secondary phases in Figure S2 in the Supporting Information), which was formed during sintering due to the volatilization of alkaline ions.[27] A secondary phase, with orthorhombic symmetry and s.g Pnma, was also detected for $x>1$. Since this impurity phase appears for the high concentration of MN, it is reasonable to relate it to the addition of dopant, which reaches the solubility limit around $x\sim1$. The diffraction peaks of MN could not be observed for any pattern (Figure 3a). This seems in apparent contrast with the post calcined KNN-xMN patterns, which presented the Bragg reflections ascribable to MN phase (see Figure S3 in the Supporting Information). The disappearance of the MN peaks is then related to the full reaction between KNN and MN, which took place during the sintering process.

The patterns of sintered samples have been analyzed by the Rietveld method and the results are shown in Table 1. As it can be surmised, the single-phase homogeneity was obtained during the subsequent sintering step at 1100 °C, with the formation of a with formula $K_{0.5}Na_{0.5}NbO_3$. Cell parameters and cell volume turn out to be in good agreement with the literature data (Table 1). The system with 0.5 wt.% of MN (KNN-0.5MN) showed a similar crystalline structure with a dominant orthorhombic Amm2 phase, while the Rietveld analysis performed on the KNN-1MN pattern, revealed the presence in trace (~3 wt.%) of the orthorhombic Pnma secondary phase. This still unknown phase possesses a $KTiNbO_5$-type structure, also observed in other ceramics such as $Rb(Mg_{0.34}Nb_{1.66})O_5$ and $K(Fe_{0.43}Nb_{1.57})O_5$ and, as already mentioned above, its presence is probably related to the solubility limit of MN in KNN ceramics and/or volatilization and segregation of alkali elements during the thermal treatment.[28] Increasing the content of MN (KNN-2MN), a further increase of this second phase has been detected (~5 wt.%). The results show that the crystallographic parameters of the Amm2 phase are roughly similar for all samples (Table 1). However, as it can be better visualized in the magnification in Figure 3b for the (022) and (200) reflection peaks, a slight shift toward higher two theta angles, for increasing amount of MN, has been observed. Since the ionic

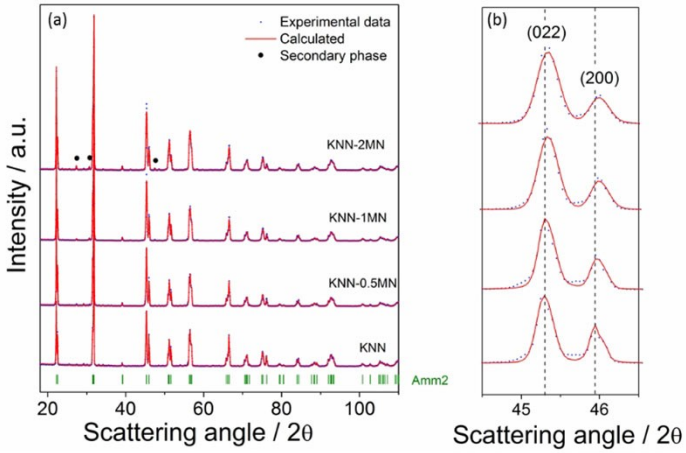

Figure 3. (a) XRD pattern and Rietveld refinement of KNN-xMN sintered pellets. (b) magnification of the (022) and (200) reflection peaks between 44.5 and 46.5°.

Table 1. Structural parameters estimated by Rietveld analysis on sintered KNN powders XRD patterns. In [27] the Bmm2 settings are interchanged with Amm2 for comparison purposes.

Sample	Phase (SG)	a [Å]	b [Å]	c [Å]	V [Å]	r.m.s strain	wt. [%]	Rwp [%]
KNN	*Amm2*	3.9476	5.6439	5.6755	126.449	$6.0*10^{-4}$	98	10.27
	P4/mbm	12.5866		3.9729	629.397	$5.4*10^{-4}$	2	
KNN-0.5MN	*Amm2*	3.9466	5.6422	5.6744	126.355	$1.4*10^{-3}$	97	10.85
	P4/mbm	12.5925		3.9714	629.749	$2.1*10^{-4}$	3	
KNN-1MN	*Amm2*	3.9451	5.6406	5.6719	126.215	$1.5*10^{-3}$	97	10.25
	Pnma	6.5279	3.8250	18.6057	464.570	$8.7*10^{-4}$	3	
KNN-2MN	*Amm2*	3.9453	5.6410	5.6711	126.213	$1.8*10^{-3}$	95	10.38
	Pnma	6.5313	3.8255	18.6145	465.092	$7.0*10^{-4}$	5	
KNN[27]	*Amm2*	3.9436	5.6510	5.6726	126.415			

radius of Mg^{2+} (0.72 Å, 6 CN) is larger than Nb^{5+} (0.64 Å, 6 CN), the addition of a low amount of Mg^{2+} inside the KNN matrix is expected to produce an expansion of the unit cell, as observed by Li and co-authors.[29] For higher amount of Mg^{2+} this effect is limited by the high oxygen vacancy concentration which produces a reverse tendency and thus a shrinkage of the unit cell. In this case, a decrease in the cell volume is observed with an increasing concentration of MN. This phenomenon could be explained by the formation of A-site vacancy in the ABO_3 perovskite formula, due to the addition of an excess of Nb^{5+} ions (B-site) which causes an overall decrease in the cell volume. Similar behavior was found for KNN modified with another columbite-type structure dopant as $CuNb_2O_6$.[30] The equivalent cell volume for KNN-1MN and KNN-2MN, further confirms that the solubility limit of MN in the KNN matrix is roughly $x \sim 1$. Furthermore, the root-mean-square strain (r.m.s strain), which is a measure of the lattice distortion, for the Amm2 phase increases as a function of the amount of MN. Pure KNN shows a strain of about $6.0*10^{-4}$ (Table 1) while KNN-2MN has a strain of about $1.8*10^{-3}$, which is one order of magnitude higher than pure KNN.

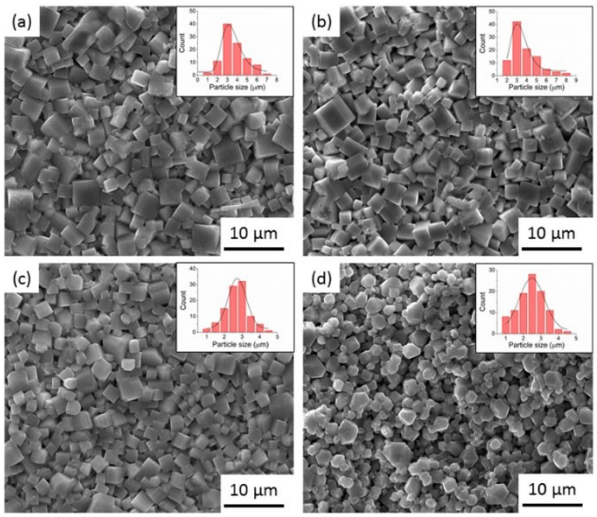

Figure 4. SEM micrographs of selected areas for grain size analysis (a) KNN, (b) KNN 0.5MN, (c) KNN-1MN and (d) KNN-2MN sintered at 1100 °C for 3 h. Insets shows the grain size distributions.

The SEM micrographs of surfaces of the KNN-xMN ceramics sintered at 1100 °C, are illustrated in Figure 4. The images show that the pure KNN and KNN-0.5MN (Figure 4a and Figure 4b) reveal a similar microstructure characterized by cubic-shape grains.[31] The KNN-1MN (Figure 4c) presents a well-packed microstructure characterized by a more homogeneous grain size. An evident limit of the grain growth was reached for the KNN-2MN sample, which showed a less compact microstructure, an increase of porosity and roundish grain morphology (Figure 4d). This evidence suggests that an excess of the orthorhombic Pnma secondary phase, most probably located at grain boundaries, inhibits the growth of the grains, also preventing the formation of cubic grains. The statistical calculation of the grain size reveals that KNN and KNN-0.5MN have a lognormal grain distribution with an average grain size of 3.38 µm and 3.25 µm, respectively. For a high amount of MN ($x > 1$) large particles of > 6 µm are not detected anymore and the grain size distributions, both for KNN-1MN and KNN-2MN, are characterized by a narrower, quasi-Gaussian curve, with an average grain size of 2.72 µm and 2.48 µm, respectively.

A similar behavior for higher amount of the impurity phase, has been observed in other ceramics systems, such as Mn-doped $BiFeO_3$ and $KCuTa_3O_9$-modified KNN.[32]

Figure 5 shows the dielectric permittivity and losses of KNN-1MN and KNN-2MN as a function of the temperature for increasing frequency from 1 kHz. The low temperature (T1) dielectric anomaly corresponds to the orthorhombic to tetragonal (O-T) polymorphic phase transition, whereas the high temperature (T2) corresponds to the phase transition to the paraelectric cubic phase (T-C). KNN-0.5MN ceramic has similar temperature dependence as KNN-1MN one (Figure 5) with well-defined anomalies. T1 takes place at 175.7, 175.8 and 94.4 °C, for KNN-0.5MN, KNN1-MN and KNN-2MN at 1 kHz, respectively, and is always lower than the one for pure KNN (200 °C).[6] Thus, the decrease of T1, as the amount of MN increases, is not linear. For KNN-2MN this low-temperature anomaly is much wider. This diffuse phase transition could reflect the crystal disorder confirmed by XRD analysis, in turn reflected in the distinct morphology of the grains in this ceramic (Figure 4d). T2 for the maximum permittivity is 396.1, 400.0 and 413.8 °C at 1 kHz, for 0.5, 1 and 2% of MN, respectively. All temperatures are also lower than that for pure KNN (420 °C).[6] This reduction of temperatures is also found for other dopants.[19] The higher

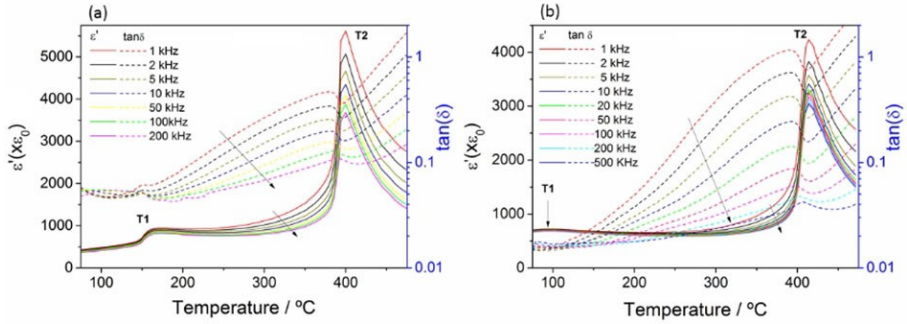

Figure 5. Dielectric permittivity ε^{T}_{33} and losses vs. temperature for (a) KNN-1MN and (b) KNN-2MN ceramics. Arrows indicate increasing frequency.

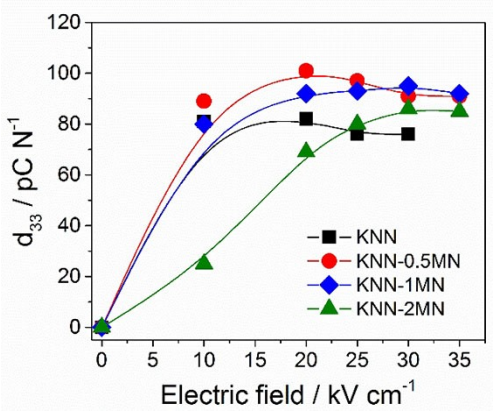

Figure 6. Piezoelectric coefficient d_{33} Vs Electric field.

porosity of the KNN-2MN ceramic gives place to a lower value of the maximum permittivity at T2.

Figure 6 shows d_{33} as a function of the electric poling field. We can see that the KNN-0.5MN sample shows the highest d_{33} value for 20 kV cm^{-1}. The threshold value, beyond which the d_{33} starts to decrease due to the mechanical deterioration of the sample, seems to be 20 kV cm^{-1} for the pure KNN and KNN-0.5MN. The KNN-1MN shows endurance against degradation by electric field until 30 kV cm^{-1}, though the saturation of d_{33} is reached at 20 kV cm^{-1}.

This behavior is most probably related to the increase in the amount of additive, which results in better densification and optimized microstructure for KNN-1MN (Figure 4c). The pure KNN and KNN-0.5MN continue to worsen while KNN-2MN undergoes the degradation only after the maximum d_{33} is achieved at 30 kV cm^{-1}. In Figure 6 is apparent that the increase of MN content above 1% makes it necessary to use higher poling fields to achieve similar, slightly lower, d_{33}. This slightly lower value is most likely a microstructural effect of the higher porosity of the ceramic (Figure 4d). In KNN-2MN, the need of a higher field to get almost similar d_{33} is mainly due to the lower grain size of this sample. It is well-known that the ferroelectric domain width is proportional to the grain size. The more complex domain configuration and the higher surface pinning of domain walls, causing their reduced mobility, results in higher energy needed for their reorientation, thus higher electric fields.[33] The inhibition of grain growth, as already explained, is a compositional effect.

Table 2 shows a comparison between some properties of the ceramics in our work with the higher d_{33} values (Figure 6) and ceramics of KNN doped with common sintering aids, such as Cu and Zn based compounds. Cu-doped ceramics show a much higher mechanical quality factor (Q_m) than the ceramics here studied due to what appears to be a major electromechanical "hardening" effect of Cu-based compounds, however Q_m values are comparable with those of Zn-based compounds.[19,34–36] However, the piezoelectric coefficient (d_{33}), planar coupling factor (k_p), relative dielectric permittivity (ε^T_{33}) and dielectric losses ($\tan\delta_e$) are comparable.

All piezoelectric, elastic and dielectric complex parameters obtained from the radial resonance of the ceramics studied in this work are shown in Table 3. As a representative example, Figure 7a shows the measured complex impedance curves (modulus and phase) for the fundamental mode of the extensional radial resonance of a thin disk of KNN-0.5MN ceramic. Figure 7b also shows the equivalent plot of R and G, both the experimental and reconstructed peaks, used for the calculation of parameters in Table 3. It is apparent that the model used is accurate and reproduces well the experimental curves (Fig-

Table 3. Room temperature piezoelectric, dielectric and elastic complex material properties of KNN-xMN ceramics.

Property/Sample	KNN	KNN-0,5MN	KNN-1MN	KNN-2MN
d_{33} (pC N^{-1})	78	97	92	85
R^2	0.99995	0.99858	0.99976	0.99782
d_{31} (pC N^{-1})	−19.32	−36.99	−31.90	−29.60
$Q_p(d_{31})$	105	76	47	107
d_{33}/d_{31}	4.03	2.62	2.88	2.93
g_{31} (10^{-3} mV N^{-1})	−8.85	−14.04	−10.8	−8.47
$Q_p(g_{31})$	416	69	45	141
N_p (kHz mm)	3320	2399	3071	3298
k_p (%)	21.60	27.36	29.06	26.42
k_{31}	13.34	15.72	17.25	14.79
ε^T_{33}	247	297	334	395
$\tan\delta_e$	0.012	0.028	0.043	0.016
s^E_{11} (pm^2 N^{-1})	9.61	21.02	11.52	11.45
$Q_m(s^E_{11})$	307	158	118	261
s^E_{12} (pm^2 N^{-1})	−2.30	−7.14	−3.41	−4.27
$Q_m(s^E_{12})$	307	158	118	261
s^D_{11} (pm^2 N^{-1})	9.44	20.50	11.18	11.00
$Q_m(s^D_{11})$	312	154	114	259
s^D_{12} (pm^2 N^{-1})	−2.47	−7.65	−3.75	−4.52
$Q_m(s^D_{12})$	283	172	131	267
s^E_{66} (pm^2 N^{-1})	23.82	56.30	29.85	31.44
$Q_m(s^E_{66})$	307	158	118	261
$c^E_{11}p$ (10^{10} N m^{-2})	11.04	5.38	9.51	10.14
$Q_m(c^{pE}_{11}p)$	307	158	118	261
c^{pD}_{11} (10^{10} N m^{-2})	11.37	5.67	10.08	10.67
$Q_m(c^{pD}_{11})$	319	148	110	256
Poisson's ratio (σ^p)	0.239	0.339	0.296	0.373
Q_s(calc)	308	152	120	249
Q_p(calc)	323	147	108	256

Table 2. Comparison of properties between ceramics in our work and of some KNN ceramics modified with common oxide.

Property/Sample	KNN-0.5MN	KNN-1MN	KNN-$K_4CuNb_8O_{23}$	KNN-CuO	KNN-CuO	KNN-ZnO
d_{33} (pC N^{-1})	97	92	90	82	86	97
k_p (%)	27.4	29.1	36	39	38	30.4
ε^T_{33}	267	282	292	240	231	371
$\tan\delta_e$	0.015	0.043	0.006	0.005	0.003	0.068
Q_m	158	116	1500	2523	2280	143
[Ref]	[This work]	[This work]	[19]	[34]	[35]	[36]

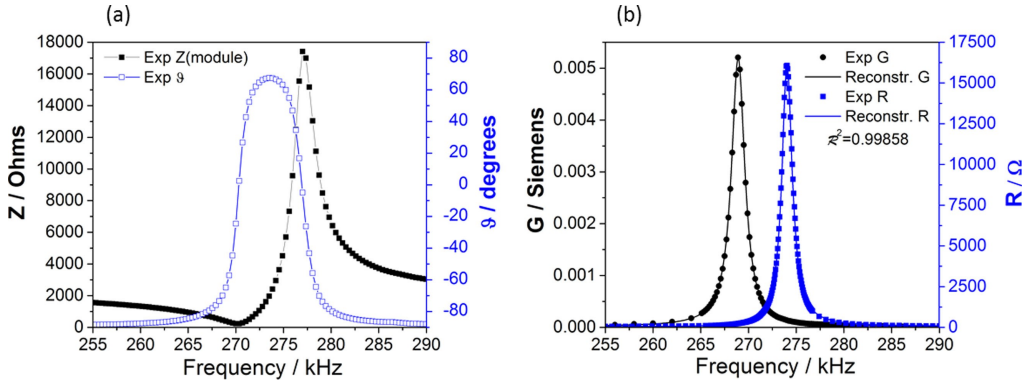

Figure 7. Equivalent representations of the complex impedance spectrum at the fundamental radial mode of resonance of a thin disk of KNN-0.5MN ceramic: (a) experimental modulus and phase plot and (b) R and G plot that is used in the iterative analysis, where symbols represent the experimental data and lines the reconstructed peaks.

ure 7b) as quantified by a R^2 factor close to 1. This happens to all ceramics (Table 3). Instead, the losses commonly reported are restricted to one dielectric ($\tan\delta_e$) and one mechanical (Q_m) factor. Piezoelectric losses arise from the friction of the vibration or strain that result as a response to an electric field or from the dielectric losses associated with the voltage or charge generated as a response of a mechanical stress.

They are an important parameter in the design of devices as they emerge as undesired hysteresis of the piezoelectric response and heat generation. What clearly emerges from Table 3 is that the addition of the doping agent increases the piezoelectric response with respect to the undoped composition. In particular, the enhancement of the charge coefficients, d_{33} and d_{31}, and coupling factors, k_p and k_{31} has been proved in the compositional range between 0.5–1 % of MN. The addition of MN also reduces the piezoelectric anisotropy as quantified by the ratio d_{33}/d_{31}. The wide low temperature dielectric anomaly of KNN-2MN (Figure 5b) influences the room temperature values of ε^T_{33}, also at the frequency of planar resonance. Permittivity at room temperature otherwise should be lower for this ceramic, since it contains higher porosity (Figure 4d), but, nevertheless, is the highest of the modified ceramics. All ceramics have higher compliances (s_{ij}), as well as lower stiffness (c_{ij}) and frequency number (N_p) than pure KNN, but also than the KNN-$K_4CuNb_8O_{23}$ doped ceramic, favoring the sensor performance.[19] All modified ceramics are less stiff at resonance than pure KNN. Losses are also calculated by the ratio between the frequency of the maximum of the recalculated R and G peaks and their width at half height, Q_s and Q_p, respectively, as losses affect the shape of these peaks. In this way the R, G peak plots are the fingerprint of the losses of the ceramic. Noticeably, Q_s correlates very well with the $Q_m(s^E_{ij})$ mechanical quality factors. The KNN-0.5MN sample shows the best piezoelectric activity and relatively low piezoelectric losses ($d_{33}=97$ pC N^{-1}, $d_{31}=-36.99$ pC N^{-1} and $g_{31}=-14.04\times10^{-3}$ mV N^{-1}; $Q_p(d_{31})=76$ (or $\tan\delta_p$ $(d_{31})=0.013$) and $Q_p(g_{31})=69$ (or $\tan\delta_p(g_{31})=0.015$), which results in the best sensor performance for charge and voltage generation. KNN-0.5MN ceramic is also the most compliant. KNN-1MN shows the best coupling factors (kp= 29.06% and $k_{31}=17.25$%), which means the best energy conversion efficiency, which is related with the best microstructure achieved (Figure 4c).

3. Conclusions

In this work lead-free $K_{0.5}Na_{0.5}NbO_3$-x$MgNb_2O_6$ ceramics (KNN-xMN) were successfully synthesized through an easy scalable conventional solid-state method. The effect of MN on KNN matrix has been evaluated. The sintered pellets show a perovskite structure with orthorhombic symmetry and Amm2 space group. An orthorhombic Pbcm secondary phase appears for concentration of MN higher than 1.0 wt.%. Furthermore, the addition of MN causes an increase of the lattice distortion of the Amm2 phase. Experimental results show that the densification of KNN ceramics can be significantly improved by adding an appropriate amount of MN (1 wt.%). KNN-1MN also shows a better microstructure, characterized by well packed grains with narrower, quasi-Gaussian, size distribution. The Pnma secondary phase seems to act as an inhibitor of the grain growth: in fact, the KNN-2MN sample shows smaller particle size and different particle shape characterized by roundish grains. A non-linear dependence of the phase transition temperatures T1 (O-T) and T2 (T-C) with the amount of MN was found. The addition of $MgNb_2O_6$ reduces both temperatures with respect to those of pure KNN. The best properties were obtained in the compositional range between 0.5–1 wt.% of MN. KNN-0.5MN shows the highest charge and voltage coefficients with relatively lower anisotropy and piezoelectric losses ($d_{33}=97$ pC N^{-1}; $d_{31}=-36.99$ pC N^{-1} and $g_{31}=-14.04\times10^{-3}$ mV N^{-1}; $Q_p(d_{31})=76$ and $Q_p(g_{31})=69$), while KNN-1MN possess the best electromechanical coupling factors ($k_p=29.06$% and $k_{31}=17.25$%), which can be correlated with the best microstructure achieved. This work provides a positive evaluation of the addition of MN on KNN ceramics. The simple manufacturing method is easily scalable and suitable for medium-large scale productions. Further optimization of the milling and sintering conditions could lead to even better electromechanical properties and higher densities.

Experimental Section

Synthesis and Sintering of Ceramics

KNN powders were prepared through solid-state reaction, starting from a mixture of K_2CO_3 (Sigma Aldrich, $\geq$99.995%), Na_2CO_3 (Sigma Aldrich, $\geq$99.5%) and Nb_2O_5 (Alfa Aesar, 99.9985%), in a molar ratio 1:1:2, respectively. Manipulations of the starting reagents have been conducted in an Ar Glove box machine (MBraun) with level of oxygen and moisture below 2 ppm, in order to prevent hydration, contamination and side reactions. 8 grams of powders were transferred into a stainless-steel vial together with 1 ball (stainless steel) of 10 g. The powders were mechanically treated for 12 hours at 875 rpm by using a Spex 8000 M Mixer/Mill and then transferred into an alumina crucible. The calcination step was conducted from room temperature to 825 °C for 4 hours using a heating rate of 3 °C/min and then cooled up to 25 °C with a cooling rate of 10 °C/min. $MgNb_2O_6$ powders were synthesized through solid-state reaction exploiting a similar procedure reported in the current literature.[37] MgO (Sigma Aldrich, $\geq$99%) and Nb_2O_5 (Alfa Aesar, 99.9985%) in a stoichiometric molar ratio 1:2, were mixed by high energy ball-milling (Spex 8000 M Mixer/Mill), for 24 hours at 875 rpm, and then thermally treated up to 1000 °C (dwell time: 1 hour) by using a heating rate of 5 °C min^{-1} (the cooling step was realized with a rate of 10 °C min^{-1}). The corresponding X-ray diffraction pattern and Rietveld analysis are reported in Figure S4 in the Supporting Information. The modification process of KNN powders, was made by mixing appropriate amount of KNN and MN: four samples were prepared with increasing weight percentage of MN (0, 0.5, 1, 2 and 4 wt.%, respectively). KNN and MN were milled, with 5 ml of ethanol (Sigma Aldrich, purity >95%), for 24 hours at 875 rpm. The as-obtained slurry was then transferred in a beaker and heated in an oven at 150 °C for 4 hours to eliminate the solvent. The powders were finely ground in a mortar to obtain a fine particulate and mixed with few drops of polyvinyl alcohol (PVA) solution (3 wt.%) before compacting into a disk by means of a hydraulic press (220 kg min^{-2} for 30 minutes). The pellets were thermally treated for 10 hours at 550 °C to eliminate all traces of PVA. Sintering was conducted at 1100 °C for 3 hours using a heating rate of 5 °C min^{-1} and cooling rate of 10 °C min^{-1}. Finally, bulk densities were measured by geometric method.

Structural, Microstructural and Morphological Characterization

Structural investigations were conducted using a SMARTLAB diffractometer with a rotating anode source of copper (λ = 1.54178 Å) working at 40 kV and 100 mA. The spectrometer is equipped with a graphite monochromator and a scintillation tube in the diffracted beam. The patterns were collected in the angular range from 18° to 110° with a step size of 0.05° and a fixed counting time of 4 seconds per point. Quantitative analysis of the crystalline phases and structure determinations were performed with the MAUD software (Materials Analysis Using Diffraction), a Rietveld extended program.[38] Lattice parameters of the constituent phases were refined from the line peak positions after allowing a correction for the zero-offset, while crystallite size and lattice disorder contributions to the peak broadening were separated because of the wide angular range explored. Microstructure and morphology of the samples have been characterized by Quanta FEI 200 scanning electron microscope (SEM). Grain size distributions of the sintered pellets, evaluated on 100 grains, were estimated using the ImageJ software.

Piezoelectric, Dielectric and Elastic Characterization at Resonance

To measure electric properties, pellets were reduced in thickness by polishing to the proper thickness/diameter aspect ratio. Silver paste was attached on both surfaces of the thin disks and sintered at 400 °C for 30 minutes. After that, samples were increasingly poled in thickness under 10–35 kV cm^{-1} at 130 °C for 15 minutes in a silicone oil bath, followed by field cooling (FC). Permittivity vs. temperature curves at frequencies above 1 kHz were measured using an automatic temperature control and capacitance-loss tangent data acquisition from an impedance analyzer (HP 4194 A). The quasi-static d_{33} piezoelectric charge coefficient, which characterizes the sensor performance of the ceramic in the poling field direction, was measured with a Berlincourt d_{33}-meter at 100 Hz. Complex impedance as a function of the frequency was measured with an impedance analyzer (HP 4192 A-LF) at the radial extensional resonance of the thickness poled thin disks. The related piezoelectric, dielectric and elastic material coefficients, including all the losses, were determined using the software for automatic iterative analysis of the complex impedance vs. frequency curves. The numerical method used was developed by Alemany et al.[39,40] A set of non-linear equations, which result when experimental data of complex impedance (Z*) or admittance (Y* = 1/Z*) at specific frequencies are introduced into the appropriate analytical solution of the wave equation, is solved iteratively until a convergence criterion is fulfilled. This set of equations is established for as many frequencies, which are automatically selected by the program, as unknown material coefficients. For the automatic determination of these frequencies, the program uses an alternative representation to the classical plots for Z* or Y* of modulus and phase as a function of the frequency. Instead, the peaks of resistance (R) and conductance (G) values are plotted vs. frequency, being Z* = R + iX and Y* = G + iB. The two main frequencies, f_s and f_p, used to establish the set of four equations to solve, are determined as those corresponding to the maximum values in the R and G peaks, respectively. For each iteration, the other two values of frequency are also determined automatically. The reconstruction of the R and G peaks is carried out once the material coefficients are calculated. The calculated coefficients are inserted in the analytical expression of the resonance and calculation of the complex admittance is performed by this model as a function of the frequency and the reconstructed peaks plotted. The residuals for these reconstructed R and G peaks to the experimental ones, quantified by the regression factor (R^2) accounts with the validity of the model for the resonance mode. The closer is the model to the experimental curves; the closer is R^2 to 1. For the planar mode, the complex material coefficients (P* = P' − iP'') directly determined in this analysis are the piezoelectric charge coefficient, d_{31}, the dielectric permittivity, ε^T_{33}, and the elastic compliances, s^E_{11} and s^E_{12}. The value of d_{31} allows analyzing the sensor performance in the perpendicular plane to the applied field, and the ratio d_{33}/d_{31} gives an insight of the anisotropy of the material. Besides, a number of other material coefficients are determined by the software from those, using well known relationships.[40] These allow us to analyze the performances of the ceramics as generator (piezoelectric voltage coefficient g_{31}) and energy transducer (electromechanical coupling factors and frequency number k_p, k_{31}, $N_p = f_s(kHz)D(mm)$, where D is the diameter of the disk). For anisotropic materials, as the piezoelectric ceramics, the Poisson's ratio (σ) depends on the direction of extension and transverse deformation. Ceramics have two σ values, for planes parallel and perpendicular to the poling direction. From the radial mode of resonance, we can calculate the latter as $\sigma P = -s^E_{12}/s^E_{11}$. A perfectly incompressible isotropic material deformed elastically at small strains would have a Poisson's ratio of exactly 0.5. Most piezoceramics exhibit values of about 0.3. In piezoceramics, σ allows also to quantify the in-plane anisotropy,

the higher the σ the lower the anisotropy and the higher the mechanical coupling between various vibrational modes. Losses can be expressed for each material complex coefficient as loss tangent factor ($\tan\delta = P''/P'$), commonly used for the dielectric coefficients, or as a quality factor ($Q = P'/P''$), commonly used for the elastic coefficients. The mechanical Q factors (Q_m) calculated by the iterative method here used was compared with that calculated according to international standard methods. The latter was considered very accurate for both low and high loss materials, as well as for low and high electromechanical coupling factor materials.[41] The calculation of piezoelectric coefficients in complex form allows obtaining piezoelectric losses, not so commonly reported, but equally important for the design of devices.

Acknowledgements

A. Iacomini, N. Senes and M. Poddighe thanks the Erasmus + grants that supported their respective stays at ICMM, CSIC (Madrid, Spain). This work and the research activity of A. I. have been supported by a PhD program, MIUR special scholarship, within the joint agreement UNICA-UNISS for the PhD program in Chemical and Technological in Sciences. This work was partially funded by the MAT2017-86168-R project of the Spanish Ministry. S. G., S. E. and G. M., acknowledge UNISS for the financial support received within the program "Fondo di Ateneo per la ricerca 2020". All authors acknowledge the CeSAR (Centro Servizi d'Ateneo per la Ricerca) of the University of Sassari for the scanning electron microscopy and X-ray diffraction investigations.

Conflict of Interest

The authors declare no conflict of interest.

Keywords: lead free compounds · mechanochemistry · piezoelectric ceramics · solid-state synthesis · sintering additives

[1] S. Troyler McKinstry, *Am. Ceram. Soc. Bull.* **2020**, *99*(1), 22–23.
[2] J. Rodel, J. F. Li. Mater, *Res. Bull.* **2018**, *43*, 576–580.
[3] C. Wang, J. Zhao, Q. Li, Y. Li, *Appl. Energy.* **2018**, *229*, 18–30.
[4] M. Vázquez-Rodríguez, F. J. Jiménez, L. Pardo, P. Ochoa, A. M. González, J. de Frutos, *Materials* **2019**, *12*, 3725.
[5] T. Zheng, J. Wu, D. Xiao, J. Zhu, *Prog. Mater. Sci.* **2018**, *98*, 552–624.
[6] S. Garroni, N. Senes, A. Iacomini, S. Enzo, G. Mulas, L. Pardo, S. Cuesta-Lopez, *Phys. Status Solidi A.* **2018**, *215*, 1700896.
[7] B. Malič, J. Koruza, J. Hreščak, J. Bernard, K. Wang, J. G. Fisher, A. Benčan, *Materials* **2015**, *8*, 8117–8146.
[8] M. E. Villafuerte-Castrejón, E. Morán, A. Reyes-Montero, R. Vivar-Ocampo, J. A. Peña-Jiménez, S. O. Rea-López, L. Pardo, *Materials* **2016**, *9*(1), 21.
[9] N. Senes, A. Iacomini, N. Domingo, S. Enzo, G. Mulas, S. Cuesta-Lopez, S. Garroni, *Phys. Status Solidi A.* **2018**, *215*, 1700921.
[10] R. Beltrami, E. Mercadelli, C. Baldisserri, C. Galassi, F. Braghin, N. Lecis, *Powder Technol.* **2020**, *375*, 101–108.
[11] C. W. Ahn, M. Karmarkar, D. Viehland, D.-H. Kang, K.-S. Bae, S. Priya, *Ferroelectr. Lett. Sect.* **2008**, *35*(3–4), 66–72.
[12] M. Matsubara, T. Yamaguchi, Ko. Kikuta, S. Hirano, *Jpn. J. Appl. Phys.* **2004**, *43*(10) 7159–7163.
[13] M.-R. Yang, C.-C. Tsai, C.-S. Hong, S.-Y. Chu, S.-L. Yang, *J. Appl. Phys.* **2010** *108*, 094103.
[14] R. Wang, S. Shibusawa, N. Miura, H. Bando, M. Itoh, *Ferroelectrics* **2010**, *385*(1) 6141–148.
[15] Z. Pan, J. Chen, L. Fan, J. Zhang, S. Zhang, Y. Huang, L. Liu, L. Fang, X. Xing, *J. Am. Ceram. Soc.* **2015**, *98*(12), 3935–3941.
[16] J. Ryu, J.-J. Choi, B.-D. Hahn, D.-S. Park, W.-H. Yoon, K.-Y. Kim, *IEEE Trans. Ultrason. Ferroelectr. Freq. Control.* **2007**, *54*, 2510–5.
[17] I.-Y. Kang, I.-T. Seo, Y.-J. Chaa, J.-H. Choi, S. Nahma, T.-H. Sung, J.-H. Paik, *J. Eur. Ceram. Soc.* **2012** *32*, 2381–2387.
[18] X. Vendrell, J. E. García, X. Bril, D. A. Ochoa, L. Mestres, G. Dezanneau, *J. Eur. Ceram. Soc.* **2015**, *35*, 125–130.
[19] S. Zhang, J. B. Lim, H. J. Lee, T. R. Shrout, *IEEE Trans Ultrason Ferroelectr Freq Control.* **2009**; *56*(8): 1523–1527.
[20] H. Meng, Y. Yang, Y. Wang, D. Wan, Q. Li, Y. Cheng, *Ferroelectrics.* **2010**, *404*(1) 105–111.
[21] H. Birol, D. Damjanovic, N. Setter, *J. Eur. Ceram. Soc.* **2006**, *26*, 861–866.
[22] D. Gao, K. W. Kwok, D. Lin, H. L. W. Chan, *J. Mater. Sci.* **2009**, *44*, 2466–2470.
[23] S. Su, R. Zuo, X. Wang, L. Li, *Mater. Res. Bull.* **2010**, *45*(2), 124–128.
[24] C.-C. Tsaietal, S.-Y. Chu, C.-S. Hong, S.-L. Yang, *Ceram. Int.* **2013**, *39*, S165–S170.
[25] H. C. Thong, C. Zhao, Z. X. Zhu, X. Chen, J. F. Li, K. Wang, *Acta Mater.* **2019**, *166*, 551–559.
[26] J. Hreščak, A. Bencan, T. Rojac, B. Malič, *J. Eur. Ceram. Soc.* **2013**, *33*, 3065–3075.
[27] F. Hussain, I. Sterianou, A. Khesro, D. C. Sinclair, I. M. Reaney, *J. Eur. Ceram. Soc.* **2018**, *38*, 3118–3126.
[28] N. Kumada, E. Iwase, N. Kinomura, *Mater. Res. Bull.* **1998**, *33*, 1729–1738.
[29] T. Li, H. Fan, C. Long, G. Dong, S. Sun, *J. Alloys Compd.* **2014**, *609*, 60–67.
[30] M.-R. Yang, C.-C. Tsai, C.-S. Hong, S.-Y. Chu, S.-L. Yang, *J. Appl. Phys.* **2010**, *108*(9), 094103.
[31] D. Jenko, A. Benčan, B. Malič, J. Holc, M. Kosec, *Microsc. Microanal.* **2005**, *11*, 572–580.
[32] T. Wang, L. He, Y. Deng, Q. Zheng, Q. Li, N. Jiang, C. Xu, X. Cao, D. Lin, *Ceram. Int.* **2017**, *43*(17), 15666–15677.
[33] Z. Cen, Y. Yu, P. Zhao, L. Chen, C. Zhu, L. Lia, X Wang, *J. Mater. Chem. C.* **2019**, *7*, 1379–1387.
[34] D. Lin, K. W. Kwok, H. L. W. Chan, *J. Phys. D* **2008**, *41*, 045401.
[35] H. Takao, Y. Saito, Y. Aoki, K. Horibuchi, *J. Am. Ceram. Soc.* **2006**, *89*(6) 1951–1956.
[36] K. Chen, J. Zhou, F. Zhang, X. Zhang, C. Li, L. An, *J. Am. Ceram. Soc.* **2015**, *98*, 1698–1701.
[37] Y. C. Liou, Y. L. Sung, *Ceram. Int.* **2008**, *34*(2), 371–377.
[38] M. Bortolotti, L. Lutterotti, G. Pepponi, *Powder Diffr.* **2017**, *32*, S225–S230.
[39] C. Alemany, L. Pardo, B. Jiménez, F. Carmona, J. Mendiola, A. M. Gonzalez, *J. Phys. D.* **1994**, *27*(1), 148–155.
[40] C. Alemany, A. M. González, L. Pardo, B. Jiménez, F. Carmona, J. Mendiola, *J. Phys. D.* **1995**, *28*(5), 945–956.
[41] L. Amarande, C. Miclea, C. Tanasoiu, *Ferroelectrics.* **2007**, *350*(1), 38–47.

Manuscript received: April 9, 2021
Revised manuscript received: July 8, 2021